Volumetric trans-scale imaging of massive quantity of heterogeneous cell populations in centimeter-wide tissue and embryo

Authors

Taro Ichimura,[1]* Taishi Kakizuka,[2] Yuki Sato,[3] Keiko Itano,[2] Kaoru Seiriki,[4] Hitoshi Hashimoto,[1,4] Hiroya Itoga,[5] Shuichi Onami,[1,5] and Takeharu Nagai[1,2,6]*

Affiliations

[1]Transdimensional Life Imaging Division, Institute for Open and Transdisciplinary Research Initiatives, Osaka University, Yamadaoka 2-1, Suita, Osaka 565-0871, Japan.

[2]Department of Biomolecular Science and Engineering, SANKEN, Osaka University, Mihogaoka 8-1, Ibaraki, Osaka 567-0047, Japan.

[3]Department of Anatomy and Cell Biology, Graduate School of Medical Sciences, Kyushu University, Maidashi 3-1-1, Higashi-ku, Fukuoka 812-8582, Japan.

[4]Laboratory of Molecular Neuropharmacology, Graduate School of Pharmaceutical Sciences, Osaka University, Yamadaoka 1-6, Suita, Osaka 565-0871, Japan.

[5]Laboratory for Developmental Dynamics, RIKEN Center for Biosystems Dynamics Research, Minatojima-minamimachi 2-2-3, Chuo-ku, Kobe, Hyogo 650-0047, Japan.

[6] Research Institute for Electronic Science, Hokkaido University, Kita 20, Nishi 10, Kita-ku, Sapporo, Hokkaido 001-0020, Japan.

*Email address: ichimura@otri.osaka-u.ac.jp, ng1@sanken.osaka-u.ac.jp

Abstract

We established a volumetric trans-scale imaging system with an ultra-large field-of-view (FOV) that enables simultaneous observation of millions of cellular dynamics in centimeter-wide three-dimensional (3D) tissues and embryos. Using a custom-made giant lens system with a magnification of 2× and a numerical aperture (NA) of 0.25, and a CMOS camera with more than 100 megapixels, we built a trans-scale scope AMATERAS-2, and realized fluorescence imaging with a lateral spatial resolution of approximately 1.2 μm across an FOV

of approximately 1.5 × 1.0 cm^2. The 3D resolving capability was realized through a combination of optical and computational sectioning techniques tailored for our low-power imaging system. We applied the imaging technique to 1.2 cm-wide section of mouse brain, and successfully observed various regions of the brain with sub-cellular resolution in a single FOV. We also performed time-lapse imaging of a 1-cm-wide vascular network during quail embryo development for over 24 hours, visualizing the movement of over 4.0×10^5 vascular endothelial cells and quantitatively analyzing their dynamics. Our results demonstrate the potential of this technique in accelerating production of comprehensive reference maps of all cells in organisms and tissues, which contributes to understanding developmental processes, brain functions, and pathogenesis of disease, as well as high-throughput quality check of tissues used for transplantation medicine.

MAIN TEXT

Introduction

Recently, life sciences have focused on comprehending the working principles of multicellular systems, spanning from basic biology to medical applications (1–5). Multicellular systems are generally complex, comprising heterogeneous cells rather than homogeneous assemblies. To understand the mechanism by which numerous cells cooperate to express the function of the entire system, it is ideal to observe all individual components within the system simultaneously during the time span of a whole phenomenon. In particular, in scenarios where a small fraction of cells in a large multicellular system may influence the fate of the population, or when distant cells and tissues operate synchronously, deducing the entire system from observations of sub-populations becomes challenging. Therefore, the trans-scale measurement of collective dynamics of all individual cells that constitute the system of interest is desired.

In response to this demand, researchers have recently reported the development of imaging methods with large field-of-view (FOV) (6–11). Whereas most of these methods are focused on observing brain activity in neuroscience using two-photon excited fluorescence (7–10), our efforts have been dedicated to developing techniques as versatile tools for studying

multicellular systems science and developmental biology. In our previous work, we proposed a fluorescence imaging system for the visible wavelength region, capable of spatially resolving individual cells within a centimeter FOV, which we named AMATERAS1.0 (A Multi-scale/modal Analytical Tool for Every Rare Activity in Singularity), enabling simultaneous observation of dynamics in the range of 10^5–10^6 cells (11). Additionally, we successfully detected less than 1% of cells with unique roles in multicellular systems and revealed how these rare cells trigger a drastic transition from unicellular to multicellular behavior in *Dictyostelium discoideum* (12). However, the imaging system had a numerical aperture (NA) of 0.12, which is insufficient for realizing volumetric observation owing to its broad depth of field (DOF). Overcoming this limitation and enabling volumetric imaging for diverse three dimensional (3D) tissues and small organisms has been a significant challenge.

In this study, we developed AMATERAS-2, a volumetric optical imaging system with approximately 15 × 10 mm^2 FOV, equivalent to that of AMATERAS1.0 (11). The key component for the enhancement is the giant 2× lens system with an NA of 0.25, which offers improved 3D spatial resolution and higher sensitivity. By incorporating novel methodologies of optical sectioning and computational sectioning, we successfully added volumetric imaging capabilities. The effectiveness of these advancements was demonstrated in imaging 1.5-mm-thick brain section blocks and conducting a 25-h time-lapse observation of vascular endothelial cells during quail embryogenesis, allowing us to trace the spatiotemporal dynamics of approximately 4.0×10^5 cells in three dimensions.

RESULT

Optical configuration and performance

AMATERAS1.0 utilized a telecentric macro lens with 2× magnification, thus allowing dynamic observation in the centimeter-FOV with subcellular resolution (11). Despite its efficacy in biological studies, its low NA (0.12) limits both its spatial resolution in the z-direction, and system brightness. To overcome these constraints and expand the possibilities for observing cell dynamics in tissues and embryos, we developed a giant lens system with an NA of 0.25, which is more than double that of AMATERAS1.0; thus, our system provides over

two times higher spatial resolution in the transverse direction (*xy*), more than four times higher resolution in the longitudinal direction (*z*), and over four times increased brightness compared with AMATERAS1.0. Fig. 1A shows the appearance of the huge lens system, consisting of an objective lens and tube lens, which constitutes the main part of AMATERAS-2. This lens system covers an image-sensor size of 44 mm diagonal and is aberration-corrected within the 44 mm large FOV in the visible wavelength region.

We constructed a wide-field epi-illumination fluorescence imaging system (Fig. 1B, Materials and Methods) using the lens systems, which we termed AMATERAS-2w. For this configuration, we utilized either a 120-megapixel CMOS camera or a 250-megapixel CMOS camera, depending on the research purpose. Both the cameras have an approximately 35 mm diagonal, thus providing an observation FOV of 17.8 mm and 17.4 mm diagonal at 2× magnification, respectively. The pixel sizes for these cameras are 2.2 and 1.5 μm, with sampling intervals of 1.1 and 0.75 μm at 2× magnification, respectively.

We installed a high-brightness LED light sources for fluorescence excitation, directing it into the objective lens through a custom-made long-pass dichroic mirror designed for GFP imaging with a cut-off wavelength of 497 nm. To ensure uniform illumination across the entire FOV, we employed a lens-let array pair. Additionally, we incorporated a 2-inch band-pass fluorescence filter between the tube lens and the camera.

We experimentally obtained the optical point spread function (PSF) using green fluorescent beads with a 0.2-μm diameter. Both the 120-megapixel CMOS camera (Fig. 1C) and the 250-megapixel CMOS camera (Fig. 1D) were employed. The left panels in Figs. 1C and D display the PSFs in the *xy* and *xz* planes, respectively. The spatial resolution was evaluated by measuring the full-width of half-maximum (FWHM) of the PSFs in the transverse direction (*xy*-direction), determined through Gaussian-function fit to the line profiles in the right panels. The resolutions obtained with the 120- and 250-megapixel cameras were comparable around 1.15 μm (*xy*). Essentially, both the CMOS cameras offered nearly the same resolution; however, owing to the coarse sampling interval in the 120-megapixel case, the apparent spatial resolution degrades when a bead is positioned on the boundary of two pixels (Figs. S1A and B).

Additional calculations and measured results are available in the Supplementary file (Fig. S1). The coarse sampling may also introduce uncertainty in the estimated position of the bead's center coordinate, varying based on the relative position of the bead and the pixel (Fig. S1E). Although this may pose some challenges in quantitatively evaluating fine shapes in cells, it is not a practical issue in imaging at cell resolution. By contrast, the 250-megapixel camera provides a nearly constant resolution (Figs. S1C and D). Thus, the 250-megapixel camera is suitable when high-resolution images are required, whereas the 120-megapixel camera is suitable for other cases where increasing the number of photons per pixel or suppressing data size is necessary.

In the depth direction (*z*-direction), we evaluated the depth of field (DOF) by fitting Gaussian curves to the line profiles (Figs. 1C and D, right bottom). The DOF was measured as 15.1 and 14.0 μm for the 120- and 250-megapixel cameras, respectively. This difference in DOF is attributed to the distinct pixel sizes of the cameras (13).

The spatial resolution in the transverse direction has been significantly improved, approximately two times compared with that of AMATERAS1.0. Figs. 1E and F display fluorescence images of cardiomyocytes derived from human induced pluripotent stem cells (hiPSCs) stained with Rhodamine phalloidin (E) across the entire FOV and (F) within a selected local region indicated by a white square in (E). These images were captured using the 250-megapixel camera, and the FOV size was 14.7×9.4 mm^2. For comparison, Fig. 1G shows an image of the same area observed with AMATERAS1.0. Evidently, AMATERAS-2w delivers more detailed images with finer spatial structures. This is further confirmed by the line profiles depicted in Fig. 1H, where the filamentous actin stained with Rhodamine exhibits a sharper spatial resolution with AMATERAS-2w.

Spinning pinhole-array disk provides optical sectioning capability in wide-FOV

This imaging system utilizes wide-field illumination and detection, which currently lacks the capability to selectively acquire images of specific *z*-planes. To extend the system's applicability, we developed two methods to enable 3D imaging, namely, optical sectioning and computational sectioning.

For optical sectioning, various options exist for achieving 3D fluorescence imaging in the visible wavelength region. These include scanning confocal microscopy (4,14), light-sheet microscopy (15), light-field microscopy (16), and spatiotemporal focusing (17). Among these options, we selected the confocal imaging method for this study owing to the limitations of light-sheet method in uniformly illuminating areas larger than 1 cm (15,18), and the trade-off between spatial resolution and the ability to resolve three dimensions in a single shot for the light-field method (19).

We considered the confocal method to be the most compatible with our imaging system. Considering the vast FOV, we adopted the multipoint-scanning confocal system. The commonly used method involving a combination of a microlens array and a pinhole array disk (20) could not be employed in AMATERAS owing to the large NA of the tube lens (NA = 0.125) compared with that of a standard microscope. Matching the NA requires shortening the distance between the two disks or enlarging the microlenses. However, shortening the inter-disk distance leads to a loss of space for inserting a dichroic mirror, and enlarging the microlenses reduces the number of foci.

To address this challenge, we opted to use pinhole arrays without microlenses herein. Although this method is less light-efficient compared with the one using microlenses, it aligns well with our imaging system's high NA and low magnification. Commercially available confocal systems using pinhole-array disks typically have large pinhole sizes (*e.g.*, 50 μm) and wide spacing between pinholes (*e.g.*, 200 μm), designed for general microscopes. For AMATERAS-2, with its 2× magnification and NA of 0.25, we required smaller pinhole sizes. As a prototype, we set the pinhole size to 6 μm (Fig. 2A), slightly larger than the diameter of the Airy disk of the PSF at green wavelengths. The optimum pinhole spacing was chosen as 24 μm, striking a balance between throughput and crosstalk (Fig. 2A). To implement this, we custom-made a pinhole-array disk and incorporated it into a rotary machine.

We positioned the pinhole array disk at the image plane of the tube lens and constructed a relay lens system to transfer the plane to the camera. This particular configuration, termed AMATERAS-2c, is illustrated in Fig. 2B (Materials and Methods). To split the light paths of

fluorescence excitation light, we placed a short-pass dichroic mirror beneath the disk. For fluorescence excitation, we used a high-brightness LED with a center wavelength of 470 nm, the same as in the wide-field imaging system (Fig. 1B). The relay lens consisted of a telecentric macro lens with 1× magnification, and a 2-inch band-pass fluorescent filter was positioned at the entrance of the macro lens. If necessary, the relay lens can be replaced by a 2× magnification lens to switch the total magnification from 2× to 4×, based on resolution requirements.

Fluorescence images of 0.5 μm fluorescent beads were observed with and without the pinhole-array disk, where fluorescent beads were three-dimensionally dispersed in an agarose gel slab (Fig. 2C). The presence of the pinhole-array disk dramatically suppressed background light from outside the focal plane. This verified that optical sectioning can be achieved by the pinhole-array disk. Typical 3D PSF was obtained with the fluorescence beads with the relay lens of (D) 1× and (E) 2× magnifications (Figs. 2D and E). As NA of the 1× relay lens (NA = 0.079) is lower than the that of the tube lens (NA = 0.125), the lateral spatial resolution (Fig. 2D) is degraded compared with the one obtained without the relay lens (Figs. 1C and D). By contrast, the 2× relay lens (NA = 0.12) almost matches with the tube lens, and the reduction in the lateral spatial resolution is relatively small (Fig. 2E).

Computational sectioning provides pseudo-depth-resolved imaging capability

In addition to optical sectioning, we developed a computational sectioning method to separate images of the focal plane and out-of-focal planes. During measurement, a *z*-stack is acquired in the wide-field imaging configuration (Fig. 1B) by scanning the focal position in the *z*-direction and capturing images at each step. The raw image in a 3D volume results from the superposition of in-focus and out-of-focus plane images. We estimated the contribution from out-of-focus planes as the baseline by iteratively applying low-pass filtering under the assumption that the image's spatial frequency in the focal plane is high.

To demonstrate computational sectioning, we observed myocardial organoids derived from hiPSCs (21). This 3D dome structure of a cavity chamber is extensively studied in developmental biology and regenerative medicine as a model for human myocardial tissue development (22,23). We fabricated a large area of organoids across the entire FOV, chemically

fixed and immunostained them for cardiac troponin T (cTnT) with Alexa488, and stained the nuclei with Hoechst33342 (Materials and Methods). The *z*-stack was obtained within a *z*-range involving the organoids (approximately 250 μm) with 4-μm intervals. Figs. 3A and B display two-color overlaid images of the island-formed organoids across the entire FOV, without and with computational sectioning, respectively (both are maximum-intensity projection (MIP) images of the *z*-stacks). Figs. 3C and D present images of six layers in the *z*-direction of the dashed square region of Figs. 3A and B, before and after computational sectioning, respectively. After the sectioning, the distribution of cTnT and nuclei in each *z*-layer is clearly visualized (Fig. 3D): The island areas are composed of multilayered cells, and the inter-island spaces are covered with a single layer of cells, as shown in Fig. 3D, z = 20 μm. A 3D isosurface representation (Fig. 3E) shows that the hollow oval structure is formed by a thin layer of cTnT-positive cells whereas the underlying cell layer is composed of cTnT-negative cells, consistent with previous literature (21). This demonstration validates the technique for wide-field imaging. Video files of Figs. 3C–E are available in the Supplementary files (Movies S1 and S2).

In principle, the signal component can be extracted as long as the signal intensity (in-focus component) is significantly higher than the statistical noise of the background intensity (out-of-focus component). This method is effective in cellular imaging when fluorescent molecules are localized within the cell, like in the nucleus, or when they exhibit a filament-like structure, thereby enabling cell recognition and dynamic tracking. It relies on the spatial frequency of the fluorescence image in the focal plane being clearly higher than that outside the focal plane.

Observing a 1.2-cm wide and 1.5-mm thick volume of mouse brain section

To demonstrate the potential for brain imaging, we performed imaging of a 1.5-mm thick mouse brain section in the coronal plane (Fig. 4A). The brain was chemically cleared using CUBIC (24,25), and the cell nuclei were stained with SYTOX-Green (Materials and Methods). The 1× relay lens was primarily employed (total magnification = 2×) to cover the coronal plane in the FOV. Each layer's exposure time was 1 s, and a total of 378 layers were acquired to cover

the entire (1.5 mm) in steps of 4 μm in the *z*-direction. Optical and computational sectioning were both applied. Fig. 4B shows a fluorescence image at a single *z*-layer (z = 700 μm), revealing the 12 mm × 8 mm wide section with single cell resolution. Fig. 4C displays enlarged views of the *xy*-plane (coronal plane) in the dashed square region, along with *xz* (transverse plane) and *yz* (sagittal plane) cross sections, essentially demonstrating successful *z*-direction sectioning. Fig. 4D shows a 3D representation of the same volume of raw data obtained by optical sectioning alone, prior to computational sectioning. However, owing to intense background light overlapping, individual cells are challenging to distinguish, particularly in regions of high cell density. By utilizing computational sectioning to eliminate background light, clear images were obtained even in areas with strong background light. Supplementary files contain videos of the z-scan for the entire FOV and local regions (Movies S3 and S4).

Fig. 4C visualizes the characteristic 3D structures of several regions, including hippocampal dentate gyrus, medial habenula, and choroid plexus, which are known to be associated with memory formation (26), depression (27), and regulation of cerebrospinal fluid (28), respectively. Close-up views of the hippocampal region in the *xy* and *xz* planes are shown in Figs. 4E and F, respectively. A comparison of the images at 2× and 4× magnification in Figs. 4E and F reveals that the higher magnification (4×) allows for improved spatial resolution and separation of individual cells in both the *xy* and *xz* planes.

Fig. 4G presents a 3D view of capillary network of the choroid plexus region, featuring three z-layer images with a difference of 20 μm in the 3D volume. The images illustrate distinct structural changes depending on their *z*-directional position. Fig. 4H shows an isosurface representation of nuclei within a cubic volume of 200 × 200 × 200 μm^3. Despite the lower resolution in the *z*-direction, the individual nuclei are spatially separated from the surrounding nuclei in the 3D space.

Dynamics of over a 4.0 x 10^5 cells were captured over 24-hours development of a quail embryo

We employed the imaging methods described for a time-lapse observation of cell migration during quail development. The non-confocal optical configuration (AMATERAS-2w, Fig. 1B)

and utilizing computational sectioning alone were sufficient for this 250-μm thick sample. We used a tie1:H2B-eYFP transgenic quail embryo (29) in which enhanced yellow fluorescent protein (eYFP) visualizes the nuclei of vascular endothelial cells (Materials and Methods). The embryo was cultured *ex ovo* on a 35 mm glass-bottom dish (Fig. 5A). Time-lapse fluorescence imaging began at 36 h (HH10) after the start of egg incubation and captured eYFP signals in the developing embryo over 24 h. For 3D imaging, we acquired *z*-stacks every 7.5 min, with each *z*-stack containing 21 layers spaced 12 μm apart. This resulted in a total of 4200 image layers and 200 time-points, with a data size of approximately 500 GB. During the time-lapse observation, we stabilized the relative distance between the lens and the sample using a self-developed autofocus system (Materials and Methods).

Representative images of cell distribution based on the nuclear eYFP signals at four time-points (t = 0, 8, 16, and 24 h) are shown in Figs. 5B and C. The figures use the HSB color model to represent the 3D distribution. The brightness indicates the intensity of the MIP image in the z-direction, whereas the hue represents the z-position with the maximum value in the MIP process (Methods). As observed in Figs. 5B and C, the cell nuclei distribution undergoes significant changes over time, thus resulting in the formation of organs such as the ventral aortae, heart, and dorsal aortae (t = 24 h, Fig. 5C). The heart region appears blurred owing to its oscillating shape caused by beating. Supplementary files include videos of the HSB-color images in the entire FOV and magnified local regions (Movies S5–S7). Fig. 5D shows enlarged views of the ventral aortae (indicated by the left dashed square in Fig. 5C) at the four time-points. Additionally, a 3D isosurface of the *z*-stack of the dorsal aorta region (the right dashed square in Fig. 5C) was calculated (Fig. 5E, and Movie S8), clearly showing the developmental process of the two tube structures of the dorsal aortae (30). Note that the upper vessel wall is partially missing in the second half of the movie because the fluorescent image was disturbed by the blood flow that began around t = 15 h.

At the current spatiotemporal resolution, we successfully traced the movement of individual cells. Segmentation of cell nuclei allowed us to detect approximately 4.5×10^6 cells across all 200 frames, and by linking cells in close proximity over consecutive frames, we tracked about

4.0×10^5 cells. Figs. 5F and G show cellular movement along with a feature parameter related to cell movement at t = 8 h and 16 h. Both left panels are magnified views of the square regions in the right panels, with trajectories drawn on MIP images. By analyzing the cell segmentation and tracking results, various feature parameters related to cell nucleus morphology and dynamics were computed, including nuclear size, brightness, aspect ratio, velocity, acceleration, mean square displacement, and meandering index (31,32). Here, we used the meandering index, a measure representing the straightness of cellular movement, to color the trajectories in Figs. 5F and G with the rainbow color table. We found that the distribution of high meandering index at t = 8 h and 16 h was significantly changed. Further detailed analysis and biological interpretation employing the cell-tracking results will be discussed in a future paper.

Discussion

In this study, we presented AMATERAS-2w, a large FOV fluorescence imaging system, along with its variant AMATERAS-2c. The system is built around a newly designed giant lens with an NA of 0.25, magnification of 2×, and field number of 44 mm. This innovative lens configuration allows for imaging with an impressive spatial resolution of approximately 1.2 μm within a centimeter-scale FOV (15×10 mm^2). Notably, this FOV-to-spatial resolution ratio surpasses that of previously reported large-FOV imaging methods. The key metric "optical invariant", derived from the product of NA and FOV, has a value of 2.75 (Materials and Methods, 33), thus indicating excellent performance of the lens system. Furthermore, the "space-bandwidth product", which signifies the FOV to spatial resolution ratio achieved under real measurement conditions (considering image sensor size and wavelength), reaches 4.3×10^8 (Materials and Methods, 34). Both of these metrics significantly outperform those reported in earlier studies on large FOV imaging methods (6–10,33). Although these metrics are essential indicators of our system's performance, they do not solely determine its superiority over other large-FOV imaging systems. Variations in biological targets and additional optical performance measures (such as frame rate and imaging depth) must also be considered. Our primary focus in designing this system was to expand the FOV, i.e., maximize the number of observable cells at any instant, even at the cost of intracellular resolution. Thus, in this aspect, our system excels as an instrument for such purposes.

The spatial resolution (FWHM) of AMATERAS-2w and -2c was measured to be approximately 1.2–1.8 μm in the transverse direction (*xy*) and 13–18 μm in the longitudinal direction (*z*) through PSF measurements (Figs. 1C, 1D, 2D, and 2E). These values represent a significant enhancement compared with the previous AMATERAS version (2.3 and 64 μm, respectively) (11). The improved transverse resolution enables clearer visualization of intracellular filamentous structures (Fig. 1H). Moreover, the refinement in longitudinal resolution was more than four times greater, thus demonstrating that the expected effect was achieved with more than double NA. Depending on the object of observation, it may be debatable whether this anisotropic spatial resolution elongated along the optical axis qualifies "cellular resolution". Although this may be insufficient to resolve dense cell populations, it proves adequate for cells with only stained nuclei or those sparsely distributed, as observed in Figs. 4F, 4H, and 5E. The next step in development involves further enhancing the NA of the lens system, including the relay lens, to further improve volumetric resolution and expand the range of observable biological objects.

We successfully achieved volumetric imaging of a 1.5-mm-thick mouse brain coronal section using the multipoint-scanning confocal imaging method, along with computational sectioning and tissue-clearing (Fig. 4). This thickness corresponds to about one-tenth of the whole brain. The exposure time per image was 1 s, and data acquisition took less than 10 min. The ultimate goal is to apply this approach to enable whole-brain imaging. Unlike previous methods such as light-sheet imaging (24) and block-face serial microscopy tomography (35), which require half a day or more for whole-brain data acquisition owing to tiling images from a narrow FOV, our method can significantly reduce the acquisition time when extended to the whole brain. Nevertheless, as the thickness increases, challenges such as increased background light and larger spherical aberration arise, thus resulting in weaker focal plane images. To address these issues and realize whole-brain imaging, we propose the incorporation of a mechanism for compensating spherical aberrations in the future. Additionally, we aim to improve the pinhole array pattern design and light source intensity to enhance transmittance and increase fluorescence intensity from samples, broadening the scope of applications.

We have shown that AMATERAS-2 can perform time-lapse observation of the centimeter-sized vascular networks in the quail embryo. It is a promising tool for understanding the multicellular behavior, especially the mechanisms of tissue formation during development (1-3). In regard to the quail embryo's case, the data obtained here are the first demonstration of the dynamics of the extensive organization of the vascular network throughout the quail embryo at the single-cell level. Conventional methods of research employing traditional microscopy have selected a limited area for observation and thus had a difficulty in determining the distribution and synchronicity of cellular dynamics across the entire system. By analyzing such a huge four-dimensional data (*xyz* and *t*), we can gain insight into when and where each organ is formed, in what order, and in what interrelationships. In addition, employing this method allows us to break away from the conventional hypothesis-driven research manner and obtain new findings in a data-driven manner. This advantage can be realized not only for quail embryo but also for a variety of other species undergoing widespread and dynamic cellular events, making it a powerful tool in the study of multicellular organisms, especially in the study of tissue formation.

To further advance multicellular systems research, information on individual cell states is required in addition to cellular dynamics, therefore multiplex measurement is an essential technological challenge. Although most of the observations presented in this paper were made with monochromatic fluorescence imaging, multiplex imaging will lead to a more profound understanding if information on the distribution of cellular states can also be obtained by employing multiple fluorescent probes. This requires technological upgrades in optical filters and light sources for multicolor imaging. In addition, spatial transcriptomics has been rapidly developing in recent years and has become one of the most crucial tools for multicellular system study (5). In the near future, dynamics imaging and spatial transcriptomics for the same sample will be a very important technological integration to advance an integrative understanding of self-organization in tissue formation. Rather than simply using AMATERAS sequentially with existing spatial transcriptomics, it could be employed as an optical detection system for spatial transcriptomics to achieve extremely high throughput in the same wide FOV of cellular dynamics imaging.

Finally, let us discuss a practical challenge we encountered with our instrument, primarily related to the handling of extensive image data. In our studies, the raw data for 3D imaging of the mouse brain section and time-lapse 3D imaging of the quail embryo amounted to approximately 100 and 500 GB, respectively. However, after multiple image processing and analysis steps, a single experimental measurement resulted in several terabyte of image data. Managing such vast data proves challenging for standard computers in terms of both software and hardware capabilities. To address software limitations, we opted not to employ commercial software for data analysis. Instead, we utilized our originally developed programs, implementing certain optimizations to reduce analysis time, minimize write/read cycles, and prevent memory overflows. As for hardware, we established a data server with petabyte storage, thereby enabling efficient data sharing among collaborators from diverse research institutions physically distant from one another. The existence of this infrastructure considerably facilitated the smooth progress of collaborative research within this study. Considering the increasing significance of handling image big data, we expect methodologies for image computation to become even more critical in the future. Ideally, a comprehensive system should be developed, encompassing not only data storage and sharing but also an integrated analysis solution in the cloud. We would like to actively promote the development of such a system, essentially encompassing advancements in imaging techniques and data-handling strategies.

MATERIALS AND METHODS

Wide-field imaging system (AMATERAS-2w) configuration

We implemented our design concept by collaborating with OptoSigma Inc. (Tokyo, Japan) to manufacture a pair of giant objective and tube lenses. The objective lens is composed of 12 optical elements in 7 groups, whereas the tube lens is composed of 9 lenses in 6 groups. Both lenses are infinity-corrected, with NAs of 0.25 for the objective and 0.125 for the tube lens. They are effectively aberration-corrected within the wavelength range of 400–700 nm. By combining these lenses, we constructed an imaging system with a 2× magnification, NA of 0.25, and a 44 mm field number. To facilitate both water-immersion and dry observation, we incorporated a glass plate whose thickness can be adjusted at the lens tip. The objective lens has a focal length of 120 mm, whereas its working distance is 14 mm owing to the presence of the attachment at the tip.

For image acquisition, a 120-megapixel CMOS camera (VCC-120CXP1M, CIS, Tokyo, Japan) and a 250-megapixel CMOS camera (VCC-250CXP1M, CIS, Tokyo, Japan) were used, out of which we selected one depending on research purpose. Both the cameras have a chip size of 35 mm (diagonal). The pixel sizes of these two cameras are 2.2 µm and 1.5 µm, respectively. The sampling intervals are 1.1 µm and 0.75 µm at 2× magnification. Image data captured by the CMOS cameras are loaded into a workstation via a CoaXpress frame grabber board (APX-3664G3, Aval Data, Tokyo, Japan). After the imaging experiments, they were transferred to a network server with large storage capacity for long-term storage and data sharing among project members.

By use of the lens system and CMOS cameras, a wide-field epi-illumination fluorescence imaging system was constructed. The imaging system chassis was designed to accommodate both inverted and upright microscope geometries. For this study, all experiments were conducted using the inverted microscope arrangement. Epi-illumination was achieved using a high-brightness LED sources (SOLIS-470C and SOLIS-385C, Thorlabs, Newton, NJ), with an excitation filter (#87-800, Edmund Optics, Barrington, NJ) placed immediately after it. The illumination light was homogenized using a pair of lenslet arrays and projected onto the sample

surface. Additionally, a similar LED light source (SOLIS-525C, Thorlabs, Newton, NJ) with an illumination homogenizer was also mounted as transmitted illumination light for bright-field observation. To split the light path, we used a custom-made long-pass dichroic mirror measuring 158 mm × 120 mm × 10 mm (BK7), which was designed for fluorescence imaging of GFP with a cut-off wavelength of 497 nm. A fluorescent filter (#86-992, Edmund Optics, Barrington, NJ) was positioned in front of the camera, which was firmly attached to the imaging lens using an F-mount.

The sample stage comprises a three-axis translational movable stage and a two-axis tilt stage. Only the *z*-axis stage is motorized, utilizing an electric actuator (SOM-C13E, OptoSigma, Tokyo, Japan). For time-lapse observation under controlled conditions, we mounted a stage-top incubator (SV-141A, BLAST, Kawasaki, Japan) on the five-axis stage, providing a stable environment at 37 °C with CO_2 control. To ensure precise measurements, we enclosed the entire sample space within a dark box, shielding it from external light and temperature fluctuations.

Multipoint confocal system (AMATERAS-2c) configuration

In the multipoint confocal imaging system, we utilized a custom-made pinhole array disk with specific dimensions (pinhole size: 6 μm, spacing: 24 μm). This disk was mounted on a high-speed rotating machine (CrestOptics, Rome, Italy) and placed precisely on the image plane of the imaging lens. Alignment throughout the FOV was ensured using a translation stage (XR25P/M, Thorlabs, Newton, NJ) and tilt stage (AIS-1016B, OptoSigma, Tokyo, Japan) to adjust height and tilt. Beneath the disk, we positioned a short-pass dichroic mirror (DMSP490L, Edmund Optics, Barrington, NJ) to allow excitation light to be incident from below. The excitation light source included a high-brightness LED (SOLIS-470C, Thorlabs, Newton, NJ), an excitation filter (#87-800, Edmund Optics, Barrington, NJ), and a pair of lenslet arrays (#63-231, Edmund Optics, Barrington, NJ), together with a 75-mm lens (f = 200 mm, LA1353-A, Thorlabs, Newton, NJ) to ensure uniform illumination onto the disk. The fluorescent image was reflected by the dichroic mirror, transmitted through a fluorescent filter (#86-992, Edmund Optics), and projected onto a 120-megapixel camera using either a 1× or 2×

relay lens (LSTL10H-F and LSTL20H-F, Myutron, Tokyo, Japan). The relay lens and camera were attached with an F-mount and secured on a three-axis translational stage (PT3/M, Thorlabs, Newton, NJ). To adjust the focus, the stage for the optical axis direction was motorized using an electric actuator (SOM-C25E, OptoSigma, Tokyo, Japan).

Measurement of 3D point spread functions

To evaluate the optical performance of the imaging systems, the 3D point spread function was measured using green fluorescent beads. Fluorescent beads with a 0.2 μm diameter (FluoSphere F8811, Invitrogen, ThermoFisher Scientific, Waltham, MA) were employed in the evaluation of AMATERAS-2w (Figs. 1C-D) and those with a 0.5 μm diameter (FluoSphere F8813, Invitrogen, ThermoFisher Scientific, Waltham, MA) were employed in the evaluation of AMATERAS-2c (Figs. 2D-E). The beads were dispersed three-dimensionally in agarose gel on a glass-bottom dish, and *z*-stacks were obtained by moving the sample in the *z*-direction in 1 or 2 μm steps.

Computational sectioning

In wide-field fluorescence imaging of a 3D volume, the superimposition of a fluorescent image from the focal plane and background light from outside the focal plane is a fundamental issue. This problem is not limited to wide-field imaging but also arises in multipoint confocal imaging of thick or high-density samples. To overcome this challenge, we employed computational sectioning, an image processing technique aimed at removing the background light component. Various algorithms have been proposed (36,37), and Leica microscopes' standard software includes this functionality. In this study, we developed an original algorithm as a simple and robust method for data analysis.

The critical step in our approach involves estimating the background light component at each layer of the *z*-stack data. To achieve this, we leverage the assumption that the background light exhibits a low spatial frequency, whereas the focal plane image demonstrates a high spatial frequency. Consequently, we employ an iterative low-pass filtering technique to estimate the background light component. Specifically, as shown in Figs. S2A and B, a two-dimensional (2D) low-pass filter is applied to the raw data ($f_0(x,y)$) to obtain a smooth surface ($L_0(x,y)$). To

obtain $f_1(x,y)$, $f_0(x,y)$ and $L_0(x,y)$ are compared and the smaller one is chosen to $f_1(x,y)$ at every position (x,y), as expressed by Eq. (1).

$$f_j(x,y) = \min \left(f_{j-1}(x,y),\ L_{j-1}(x,y)\right) \tag{1}$$

where min(a,b) returns the smaller value of a and b. Next, the low-pass filter is applied to $f_1(x,y)$ to obtain $L_1(x,y)$; this process is repeated to make $L_j(x,y)$ closer to the baseline of the original image. The iteration stops when the standard deviation of the difference of $f_j(x,y)$ and $L_j(x,y)$ reaches a preset value (ε).

$$\sqrt{Var\left(f_j(x,y) - L_j(x,y)\right)} < \varepsilon \tag{2}$$

Among various methods available as 2D low-pass filters, we sequentially applied one-dimensional (1D) infinite impulse response (IIR) filter in two directions (x,y). This method is faster than other methods such as a 2D Fourier transform (38). This speed difference is especially significant when the number of pixels in an image is massive, as in the present case. We adopted Butterworth filter for spectral transmittance of IIR low-pass filter.

Culture of hiPSCs and differentiation into cardiac organoid with cavity chamber structure

hiPSC line 201B7 was routinely maintained as previously described (39) on iMatrix-511 (Matrixome, 89292) coated culture dish in StemFit medium (Ajinomoto, AK02N), and 10 μM Y-27632 (Fujifilm Wako, 030-24021) was added for the first 24 h after passage. Four days before inducing differentiation, hiPSCs were dissociated with TrypLE Select Enzyme (Thermo Fisher Scientific, A1285901) and 1.9×10^5 cells were passed into iMatrix-511 coated 12 well plate in StemFit medium supplemented with 10 μM Y-27632. After 24 h, the medium was changed to StemFit without Y-27632 and was exchanged daily for 3 days. Differentiation was initiated with the CDM3 medium (40) composed of RPMI-1640 with HEPES (Fujifilm Wako, 189-02145), 0.5 mg/ml human recombinant albumin (Sigma Aldrich, A9731) and 0.2 mg/ml L-ascorbic acid 2-phosphate (Sigma Aldrich, A8960) supplemented with 3 μM CHIR99021 (Fujifilm Wako, 038-23101) for 48 h. On day 2 of differentiation, the medium was changed to

CDM3 supplemented with 5 μM IWP-2 (Fujifilm Wako, 034-24301). From day 4 to day 8, the cells were cultured in CDM3 and the medium was changed every other day. From day 8, the medium was changed to RPMI-1640 with HEPES supplemented with 2% B27 (Thermo Fisher Scientific, 17504044) and was changed every other day. The cells were fixed in 4% paraformaldehyde (PFA; Thermo Fisher Scientific, 43368) on day 15 for immunocytochemical analysis.

Immunocytochemical staining of cardiac organoid

Cells were fixed with 4% PFA for 15 min at room temperature (RT ~23 °C), permeabilized with 0.2% Triton X-100 (Fujifilm Wako, 807423) for 20 min at RT and incubated with blocking solution composed of D-PBS with 5% BSA and 10 % FBS for 30 min at RT. Subsequently, the cells were incubated with primary antibody (1:200 rabbit IgG anti-cTnT, Bioss, bs-10648R) at 4 °C overnight. After washing three times, cells were incubated with secondary antibody (1:500 alexa488 conjugated goat IgG anti-rabbit IgG, Abcam, ab150077) for 2 h at RT. The cells were washed three times in D-PBS with 1 μg/ml Hoechst33342 (Dojin, H342). Subsequently, the cells were incubated with D-PBS and used for fluorescent observation.

Color representation of the 3D image

Figs. 5B–D show the 3D positions of the cells using the HSB (also known as HSV) color model. After applying the method described earlier to remove background light from the *z*-stack image, we conducted a maximum value intensity projection along the *z*-direction. The *z*-position of the maximum value at each *xy*-position was then recorded (Fig. S2C). The color image was reconstructed by associating the brightness and hue of the HSB table with the value of the maximum intensity and the maximum value position, respectively (Fig. S2D). For the hue table, we assigned red to blue to *z*-layer numbers ranging from 0 (z = 0 μm) to 20 (z = 240 μm).

Preparation of mouse brain section

All animal care and handling procedures were conducted with approval from the Animal Care and Use Committee of Osaka University (approval numbers R02-8-7). Our utmost efforts were made to minimize the number of animals used. Experiments involved adult male C57BL/6J mice (SLC, Shizuoka, Japan) aged between 2 and 3 mo. To ensure proper anesthesia, mice were

deeply anesthetized through intraperitoneal injection of an anesthetic cocktail containing 0.3 mg/kg medetomidine (Nippon Zenyaku Kogyo, Fukushima, Japan), 4 mg/kg midazolam (Sandoz Pharma, Basel, Switzerland), and 5 mg/kg butorphanol (Meiji Seika Pharma, Tokyo, Japan). Subsequently, anesthetized mice underwent transcardial perfusion with saline, followed by 4% paraformaldehyde (Nacalai Tesque, Kyoto, Japan) dissolved in phosphate-buffered saline (PBS). Brain tissues were then excised and immersed in a 4% paraformaldehyde solution until further use. For tissue preparation, brain tissue blocks were sliced into 1.5-mm thick coronal sections using a vibrating microtome (LinearSlicer Pro7N, Dosaka EM, Kyoto, Japan). Subsequent staining and tissue clearing involved immersion of sections in CUBIC-L (Tokyo Chemical Industry, Tokyo, Japan) for delipidation, SYTOX Green (Thermo Fisher Scientific, Waltham, MA, USA) solution (1:5,000) diluted in 20% (vol/vol) DMSO in PBS for nuclear staining, and CUBIC-R+(M) (Tokyo Chemical Industry, Tokyo, Japan) for refractive index matching, following previously established methods (25,41). After clearing, tissue sections were placed on glass bottom dishes and embedded in 2% (wt/vol) agarose gel prepared with CUBIC-R+(M) for subsequent imaging analysis.

Preparation of quail embryo

Transgenic quail line, tie1:H2B-eYFP (29) was bred in quail breeding facility at Kyushu University. Fertilized eggs were incubated at 38 °C. The staging of quail embryos was based on the Hamburger and Hamilton stages of chicken embryos (42). The animal study was approved by the Institutional Animal Care and Use Committee of Kyushu University (Authorization number: A20-019). *Ex ovo* culture was performed as previously described (43). Black filter paper was used instead of white filter paper to avoid fluorescence background.

Autofocus in time-lapse imaging

To address *z*-directional drift in the time-lapse observation of quail, we developed an original autofocus method. During the intervals between fluorescence z-images, we acquired bright-field *z*-stacks and analyzed the images to identify the most in-focus position. To achieve this, we used a black ink marker located on the substrate edge as the autofocus target instead of the variable sample itself. For evaluating the degree of in-focus, we applied a total variation

(TV) filter to the marker image and used the kurtosis of the filtered image as the focus score. The *z*-position with the maximum focus score was identified as the in-focus location, thus signifying the sharpest image of the marker edge. Although other filter types and statistical moments are available options for the focus score (44), our preliminary experiments demonstrated the suitability of the kurtosis of TV for the marker image. In the actual experiment, we acquired 15 images in 15 µm steps and plotted the focus scores against *z*-positions. Through quadratic function fitting of the focus scores at three z-positions (including the *z*-position with the maximum value and adjacent positions), we estimated the best in-focus position with an accuracy of 1 µm.

Cell segmentation and tracking

Cell location detection and tracking were conducted in this study using *z*-stack observations covering a thickness of 240 µm. An issue encountered was the overlap of multiple cells in the *z*-direction, thus potentially resulting in the loss of less intense cells when detected solely on a 2D projected image. To overcome this, 3D cell detection was considered; however, owing to the substantial data size, it proved impractical, especially with commercially available software that requires restricting the region of interest to a small size. To strike a balance between computational cost and detection accuracy, we proposed a method of dividing the *z*-stack into three blocks in the *z*-direction. Within each block, cell detection was performed on the MIP images, and the resulting cell lists were compared to identify identical cells detected across multiple blocks. By recognizing double-detected cell pairs as identical, we updated the cell list accordingly. This iterative process was applied to all double-detected cells, thus achieving effective cell detection and enabling cell tracking throughout the observation period.

Evaluation of optical system with optical invariant and space-bandwidth product

We employed two indices to evaluate the lens system's scale range and compare it with previous research. The first index, the optical invariant, measures the lens system's performance and is obtained by multiplying the FOV radius and NA. The second index, the space-bandwidth product, considers the image sensor and wavelength while quantifying the ratio of actual resolution to FOV. These indices are calculated using the following simplified formulas,

respectively (33).

$$I = \frac{NA \times FN}{2M} \qquad (3)$$

$$SBP = 8\left(\frac{R_{FOV}}{d_{xy}}\right)^2 \qquad (4)$$

where *I*, *FN*, *M*, *SBP*, R_{FOV}, and *dxy* denote optical invariant, field number, magnification, space-bandwidth product, FOV radius, and spatial resolution (FWHM).

References

1. Y. Sasai, Cytosystems dynamics in self-organization of tissue architecture. *Nature*. **493**, 318–326 (2013).
2. K. McDole, L. Guignard, F. Amat, A. Berger, G. Malandain, L. A. Royer, S. C. Turaga, K. Branson, P. J. Keller, In Toto Imaging and Reconstruction of Post-Implantation Mouse Development at the Single-Cell Level. *Cell.* **175**, 859-876.e33 (2018).
3. M. H. Dominguez, A. L. Krup, J. M. Muncie, B. G. Bruneau, Graded mesoderm assembly governs cell fate and morphogenesis of the early mammalian heart. *Cell*. **186**, 479-496.e23 (2023).
4. H. R. Ueda, H. U. Dodt, P. Osten, M. N. Economo, J. Chandrashekar, P. J. Keller, Whole-Brain Profiling of Cells and Circuits in Mammals by Tissue Clearing and Light-Sheet Microscopy. *Neuron*. **106**, 369–387 (2020).
5. A. Rao, D. Barkley, G. S. França, I. Yanai, Exploring tissue architecture using spatial transcriptomics. *Nature*. **596**, 211–220 (2021).
6. G. McConnell, J. Trägårdh, R. Amor, J. Dempster, E. Reid, W. B. Amos, A novel optical microscope for imaging large embryos and tissue volumes with sub-cellular resolution throughout. *Elife*. **5**, e18659 (2016).
7. N. J. Sofroniew, D. Flickinger, J. King, K. Svoboda, A large field of view two-photon mesoscope with subcellular resolution for in vivo imaging. *Elife*. **5,** e14472 (2016).
8. J. Fan, J. Suo, J. Wu, H. Xie, Y. Shen, F. Chen, G. Wang, L. Cao, G. Jin, Q. He, T. Li, G. Luan, L. Kong, Z. Zheng, Q. Dai, Video-rate imaging of biological dynamics at centimetre scale and micrometre resolution. *Nat. Photonics.* **13**, 809–816 (2019).
9. K. Ota, Y. Oisi, T. Suzuki, M. Ikeda, Y. Ito, T. Ito, H. Uwamori, K. Kobayashi, M. Kobayashi, M. Odagawa, C. Matsubara, Y. Kuroiwa, M. Horikoshi, J. Matsushita, H. Hioki, M. Ohkura, J. Nakai, M. Oizumi, A. Miyawaki, T. Aonishi, T. Ode, M. Murayama, Fast, cell-resolution, contiguous-wide two-photon imaging to reveal functional network architectures across multi-modal cortical areas. *Neuron*. **109**, 1810-1824.e9 (2021).

10. C. H. Yu, J. N. Stirman, Y. Yu, R. Hira, S. L. Smith, Diesel2p mesoscope with dual independent scan engines for flexible capture of dynamics in distributed neural circuitry. *Nat. Commun.* **12**, 6639 (2021).

11. T. Ichimura, T. Kakizuka, K. Horikawa, K. Seiriki, A. Kasai, H. Hashimoto, K. Fujita, T. M. Watanabe, T. Nagai, Exploring rare cellular activity in more than one million cells by a transscale scope. *Sci. Rep.* **11**, 16539 (2021).

12. T. Kakizuka, Y. Hara, Y. Ohta, A. Mukai, A. Ichiraku, Y. Arai, T. Ichimura, T. Nagai, K. Horikawa, *bioRxiv*, doi:10.1101/2020.06.29.176891.

13. H. Gross, F. Blechinger, and B. Achtner. *Handbook of Optical Systems, Volume 4: Survey of Optical Instruments* (Wiley-VCH, Weinheim, 2008).

14. G. S. Kino, T. R. Corle, *Confocal Scanning Optical Microscopy and Related Imaging Systems 1st Edition* (Academic Press, Cambridge, MA, 1996).

15. E. Battistella, J. Schniete, K. Wesencraft, J. F. Quintana, G. McConnell, Light-sheet mesoscopy with the Mesolens provides fast sub-cellular resolution imaging throughout large tissue volumes. *iScience*. **25**, 104797 (2022).

16. R. Prevedel, Y. G. Yoon, M. Hoffmann, N. Pak, G. Wetzstein, S. Kato, T. Schrödel, R. Raskar, M. Zimmer, E. S. Boyden, A. Vaziri, Simultaneous whole-animal 3D imaging of neuronal activity using light-field microscopy. *Nat. Methods.* **11,** 727–730 (2014).

17. E. Papagiakoumou, E. Ronzitti, V. Emiliani, Scanless two-photon excitation with temporal focusing. *Nat. Methods* **17**, 571–581 (2020).

18. F. F. Voigt, D. Kirschenbaum, E. Platonova, S. Pagès, R. A. A. Campbell, R. Kastli, M. Schaettin, L. Egolf, A. van der Bourg, P. Bethge, K. Haenraets, N. Frézel, T. Topilko, P. Perin, D. Hillier, S. Hildebrand, A. Schueth, A. Roebroeck, B. Roska, E. T. Stoeckli, R. Pizzala, N. Renier, H. U. Zeilhofer, T. Karayannis, U. Ziegler, L. Batti, A. Holtmaat, C. Lüscher, A. Aguzzi, F. Helmchen, The mesoSPIM initiative: open-source light-sheet microscopes for imaging cleared tissue. *Nat. Methods*. **16**, 1105–1108 (2019).

19. T. Nöbauer, Y. Zhang, H. Kim, A. Vaziri, Mesoscale volumetric light-field (MesoLF) imaging of neuroactivity across cortical areas at 18 Hz. *Nat. Methods*. **20**, 600–609 (2023).

20. A. Ichihara, T. Tanaami, K. Isozaki, Y. Sugiyama, Y. Kosugi, K. Mikuriya, M. Abe, I. Uemura, High-speed confocal fluorescence microscopy using a Nipkow scanner with microlenses for 3D-imaging of single fluorescent molecule in real time. *Bioimaging* **4**, 52–62 (1996).

21. Z. Ma, J. Wang, P. Loskill, N. Huebsch, S. Koo, F. L. Svedlund, N. C. Marks, E. W. Hua, C. P. Grigoropoulos, B. R. Conklin, K. E. Healy, Self-organizing human cardiac microchambers mediated by geometric confinement. *Nat. Commun*. **61**. 6, 1–10 (2015).

22. P. Hofbauer, S. M. Jahnel, N. Papai, M. Giesshammer, A. Deyett, C. Schmidt, M. Penc, K. Tavernini, N. Grdseloff, C. Meledeth, L. C. Ginistrelli, C. Ctortecka, Š. Šalic, M. Novatchkova, S. Mendjan, Cardioids reveal self-organizing principles of human cardiogenesis. *Cell*. **184**, 3299-3317.e22 (2021).

23. Y. R. Lewis-Israeli, A. H. Wasserman, M. A. Gabalski, B. D. Volmert, Y. Ming, K. A. Ball, W. Yang, J. Zou, G. Ni, N. Pajares, X. Chatzistavrou, W. Li, C. Zhou, A. Aguirre, Self-assembling human heart organoids for the modeling of cardiac development and congenital heart disease. *Nat. Commun*. **121**. 12, 1–16 (2021).

24. E. A. Susaki, K. Tainaka, D. Perrin, F. Kishino, T. Tawara, T. M. Watanabe, C. Yokoyama, H. Onoe, M. Eguchi, S. Yamaguchi, T. Abe, H. Kiyonari, Y. Shimizu, A. Miyawaki, H. Yokota, H. R. Ueda, Whole-brain imaging with single-cell resolution using chemical cocktails and computational analysis. *Cell*. **157**, 726–739 (2014).

25. K. Tainaka, T. C. Murakami, E. A. Susaki, C. Shimizu, R. Saito, K. Takahashi, A. Hayashi-Takagi, H. Sekiya, Y. Arima, S. Nojima, M. Ikemura, T. Ushiku, Y. Shimizu, M. Murakami, K. F. Tanaka, M. Iino, H. Kasai, T. Sasaoka, K. Kobayashi, K. Miyazono, E. Morii, T. Isa, M. Fukayama, A. Kakita, H. R. Ueda, Chemical Landscape for Tissue Clearing Based on Hydrophilic Reagents. *Cell Rep*. **24**, 2196-2210.e9 (2018).

26. T. Hainmueller, M. Bartos, Dentate gyrus circuits for encoding, retrieval and discrimination of episodic memories. *Nat. Rev. Neurosci*. **21**, 153–168 (2020).

27. M. Agetsuma, H. Aizawa, T. Aoki, R. Nakayama, M. Takahoko, M. Goto, T. Sassa, R. Amo, T. Shiraki, K. Kawakami, T. Hosoya, S. I. Higashijima, H. Okamoto, The habenula is crucial for experience-dependent modification of fear responses in zebrafish. *Nat. Neurosci*. **13**, 1354–1356 (2010).

28. N. Dani, R. H. Herbst, C. McCabe, G. S. Green, K. Kaiser, J. P. Head, J. Cui, F. B. Shipley, A. Jang, D. Dionne, L. Nguyen, C. Rodman, S. J. Riesenfeld, J. Prochazka, M. Prochazkova, R. Sedlacek, F. Zhang, V. Bryja, O. Rozenblatt-Rosen, N. Habib, A. Regev, M. K. Lehtinen, A cellular and spatial map of the choroid plexus across brain ventricles and ages. *Cell*. **184**, 3056-3074.e21 (2021).

29. Y. Sato, G. Poynter, D. Huss, M. B. Filla, A. Czirok, B. J. Rongish, C. D. Little, S. E. Fraser, R. Lansford, Dynamic analysis of vascular morphogenesis using transgenic quail embryos. *PLoS One*. **5**, e12674 (2010).

30. Y. Sato, Dorsal aorta formation: Separate origins, lateral-to-medial migration, and remodeling. *Develop. Growth Differ*. **55**, 113–129 (2013).

31. E. Meijering, O. Dzyubachyk, I. Smal, Methods for cell and particle tracking. *Elsevier Inc*. **504**, 183–200 (2012).

32. J. B. Beltman, A. F. M. Marée, R. J. De Boer, Analysing immune cell migration. *Nat. Rev. Immunol*. **9**, 789–798 (2009).

33. J. R. Bumstead, J. J. Park, I. A. Rosen, A. W. Kraft, P. W. Wright, M. D. Reisman, D. C. Côté, J. P. Culver, J. R. Bumstead, J. J. Park, I. A. Rosen, A. W. Kraft, P. W. Wright, D. Reisman, D. C. Côté, J. P. Culver, M. D. Reisman, D. C. Côté, J. P. Culver, Designing a large field-of-view two- photon microscope using optical invariant analysis microscope using optical invariant analysis. *Neurophotonics*. **5**, 025001 (2018).

34. A. W. Lohmann, R. G. Dorsch, D. Mendlovic, C. Ferreira, Z. Zalevsky, Space–bandwidth product of optical signals and systems. *J. Opt. Soc. Am. A*. **13**, 470 (1996).

35. K. Seiriki, A. Kasai, T. Nakazawa, M. Niu, Y. Naka, M. Tanuma, H. Igarashi, K. Yamaura, A. Hayata-Takano, Y. Ago, H. Hashimoto, Whole-brain block-face serial microscopy tomography at subcellular resolution using FAST. *Nat. Protoc.* **14**, 1509–1529 (2019).

36. H. -C. Lee and G. Yang, Computational removal of background fluorescence for biological fluorescence microscopy. *IEEE 11th International Symposium on Biomedical Imaging (ISBI)*, 205–208, doi: 10.1109/ISBI.2014.6867845 (2014).

37. K. Walter, F. Ziesche, Apparatus and Method, Particularly for microscopes and endoscopes, using baseline estimation and half-quadratic minimization for the deblurring of images, WO 2019/185174 A1. European Patent Office (2019).

38. P. Getreuer, A Survey of Gaussian Convolution Algorithms. *Image Process. Line*. **3**, 286–310 (2013).

39. M. Nakagawa, Y. Taniguchi, S. Senda, N. Takizawa, T. Ichisaka, K. Asano, A. Morizane, D. Doi, J. Takahashi, M. Nishizawa, Y. Yoshida, T. Toyoda, K. Osafune, K. Sekiguchi, S. Yamanaka, A novel efficient feeder-Free culture system for the derivation of human induced pluripotent stem cells. *Sci. Rep*. **4**, 1–7 (2014).

40. P. W. Burridge, E. Matsa, P. Shukla, Z. C. Lin, J. M. Churko, A. D. Ebert, F. Lan, S. Diecke, B. Huber, N. M. Mordwinkin, J. R. Plews, O. J. Abilez, B. Cui, J. D. Gold, J. C. Wu, Chemically defned generation of human cardiomyocytes. *Nat. Methods*. **11**, 855–860 (2014).

41. E. A. Susaki, C. Shimizu, A. Kuno, K. Tainaka, X. Li, K. Nishi, K. Morishima, H. Ono, K. L. Ode, Y. Saeki, K. Miyamichi, K. Isa, C. Yokoyama, H. Kitaura, M. Ikemura, T. Ushiku, Y. Shimizu, T. Saito, T. C. Saido, M. Fukayama, H. Onoe, K. Touhara, T. Isa, A. Kakita, M. Shibayama, H. R. Ueda, Versatile whole-organ/body staining and imaging based on electrolyte-gel properties of biological tissues. *Nat. Commun.* **11**, 1982 (2020).

42. V. Hamburger, H. L. Hamilton, A series of normal stages in the development of the chick embryo. *J. Morphol*. **88**, 49–92 (1951).

43. Y. Sato, R. Lansford, Transgenesis and imaging in birds, and available transgenic reporter lines. *Develop. Growth Differ*. **55**, 406–421 (2013).

44. J. M. Mateos-Pérez, R. Redondo, R. Nava, J. C. Valdiviezo, G. Cristóbal, B. Escalante-Ramírez, M. J. Ruiz-Serrano, J. Pascau, M. Desco, Comparative evaluation of autofocus algorithms for a real-time system for automatic detection of Mycobacterium tuberculosis. *Cytom. Part A.* **81 A**, 213–221 (2012).

ACKNOWLEDGMENTS

We would like to thank Prof. K. Fujita of Department of Applied Physics, Osaka University, Japan for his valuable comments on optics design. We are also grateful to Prof. S. Miyagawa, and Prof. Y. Sawa of Graduate School of Medicine, Osaka University, for their support on handling human iPS cells and valuable discussion.

Funding:

Grant-in-Aid for Scientific Research on Innovative Areas “Singularity Biology (No. 8007)” 21H00431 (YS), 18H05416 (HH), 18H05412 (SO), and 18H05410, 18H05408 (TN)

Grant-in-Aid for Transformative Research Areas (A) “Seeing through Scattering Media (No. 20A207)” 21H05590 and 23H041350 (TI)

the Research Program of "Five-star Alliance" in "NJRC Mater. & Dev." (TN)

Precursory Research for Embryonic Science and Technology (PRESTO) JPMJPR18G2 (TI)

JSPS KAKENHI JP23H00395 and JP20H00492 (HH)

AMED Brain/MINDS JP21dm0207117 (HH) and BINDS JP23ama121054 and JP23ama121052 (HH)

The Uehara Memorial Foundation (TN)

Takeda Science Foundation (TN, HH)

Core Research for Evolutionary Science and Technology (CREST) JPMJCR15N3 (TN)

RIKEN Cluster for Science, Technology and Innovation Hub (SO)

JST NBDC Grant Number JPMJND2201 (SO)

Author contributions:

Conceptualization: TI, TN

Optics design: TI, HH, TN

Optical system construction: TI

Sample preparation: TK, YS, KS, HH

Data acquisition: TK, YS, TI

Data analysis and visualization: KI, TI, TK

Construction of data share server: HI, SO

Writing—original draft: TI

Writing—review & editing: TI, TN

Competing interests:

T.I, H.H and T.N have patent applications (2021-104163(JP), 2023-077341). The authors declare no additional conflict of interests.

Data and materials availability:

All data needed to evaluate the conclusions in the paper are present in the paper and/or Supplementary Materials.

FIGURES

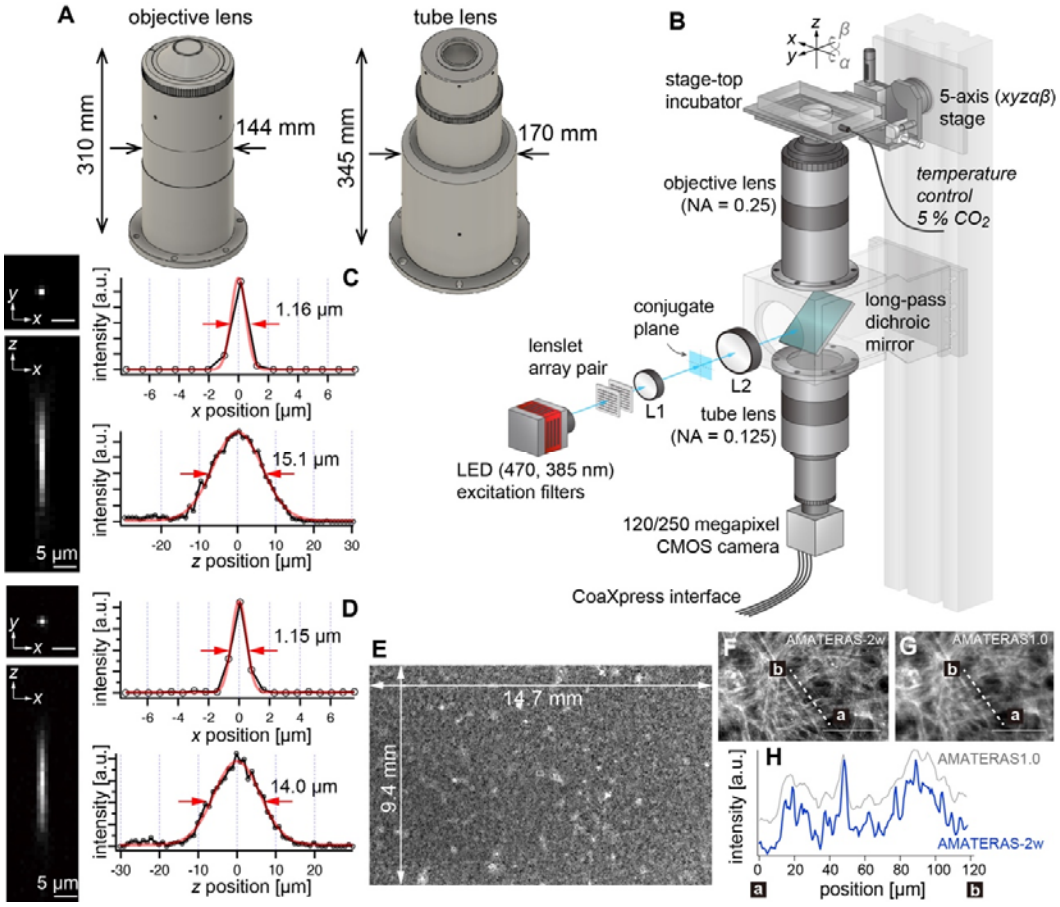

Fig. 1. AMATERAS-2w, a centimeter-FOV cell-imaging system (A) Schematics of the objective and tube lenses. (B) Schematic of the wide-field fluorescence imaging system, AMATERAS-2w, using the two lenses in (A). (C),(D) Experimentally obtained PSF of green fluorescent beads with a 0.2-µm diameter in the *xy* and *xz* planes, captured using CMOS cameras with: (C) 120 megapixels (pixel size = 2.2 µm) and (D) 250 megapixels (pixel size = 1.5 µm); the line profiles in the *x* and *z* directions on the beads are also shown with FWHMs. (E) Fluorescence image of a cardiomyocyte sheet in the entire FOV. (F) Digitally magnified view of the area indicated by a white square in (E); scale bar, 100 µm. (G) Same area as (F) but observed by AMATERAS1.0 for comparison. (H) Line profiles of the lines in (F) and (G) for comparison of spatial resolution.

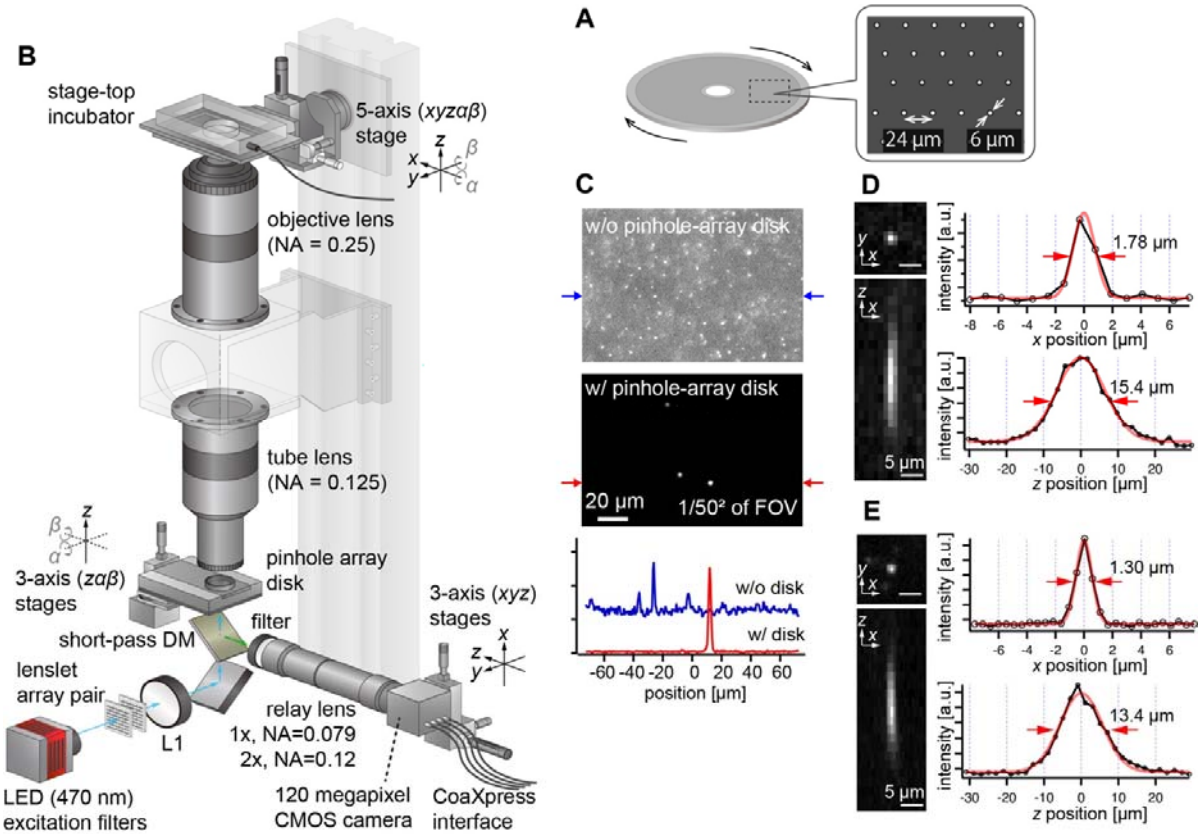

Fig. 2. AMATERAS-2c, a multipoint confocal imaging system for 3D volume imaging. (A) Design of our pinhole-array disk. (B) Schematic of the optical configuration using the pinhole-array disk. (C) Effect of background light rejection by the presence of the pinhole-array disk in a 292 × 202 µm^2 area at the FOV center corresponding to 1/50^2 of the entire FOV. (D),(E) Experimentally obtained PSF of green fluorescent beads with a diameter of 0.5 µm in the *xy* and *xz* planes, captured using relay lens with (D) 1× magnification (NA = 0.079) and (E) 2× magnification (NA = 0.12). The line profiles in the *x* and *z* directions on the beads are also shown with FWHMs.

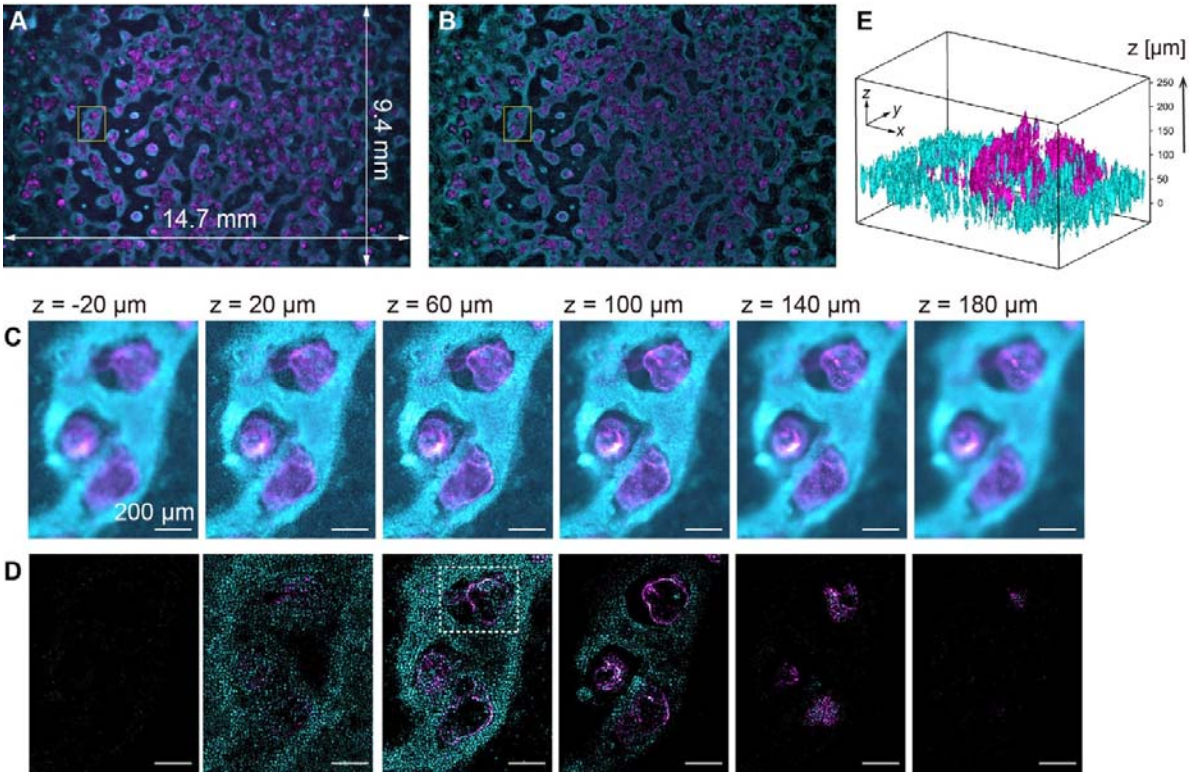

Fig. 3. Volumetric imaging with computational sectioning. (A),(B) Two-color images of the cavity chamber structure of a myocardial organoid (A) before and (B) after computational sectioning. Both (A) and (B) are MIP images of the *z*-stack data, captured using the 250-megapixel CMOS camera; here, magenta and cyan represent the distribution of immunostained cardiac troponin T and Hoechst-labeled nuclei, respectively. (C),(D) Six z-layers with a difference of 40 μm in the yellow square region indicated in (A),(B); scale bars, 200 μm. (E) Three-dimensional isosurface representation in the dashed square region indicated in (D).

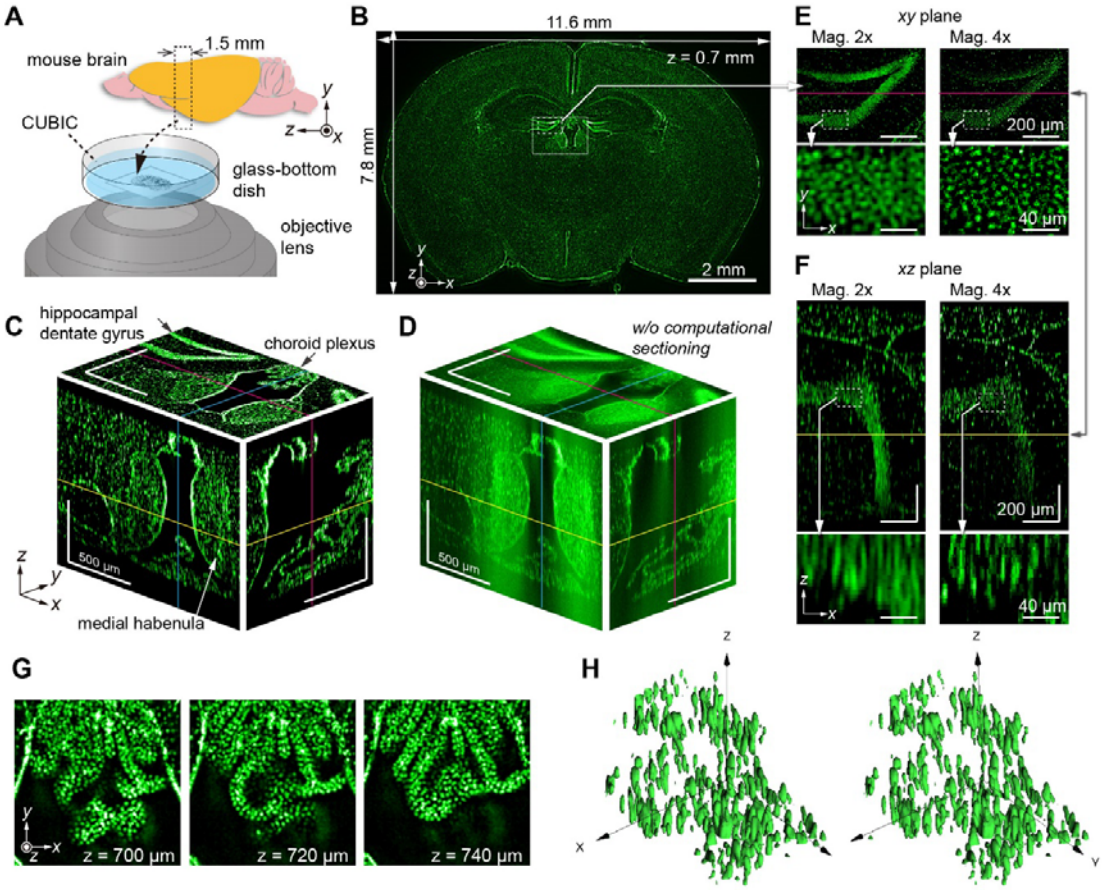

Fig. 4. Volumetric imaging of a mouse brain section. (A) Schematic of a mouse brain showing the placement of the brain sample in the inverted configuration. (B) Schematic of a single *z*-layer in the coronal plane with size of the effective area covering the entire brain section. (C) Fluorescence images of three orthogonal cross sections of the dotted square indicated in (B); here, the yellow, cyan, and magenta lines represent the *z*-, *x*-, and *y*-positions of the cross sections, respectively. (D) Cross-sectional images of raw data in the same region as (C), where the computational sectioning is not applied. (E),(F) Magnified images of the hippocampal region (dashed square in (B)) in the (E) *xy*-plane and (F) *xz*-plane. For comparison, images obtained with 2× (left) and 4× (right) magnification systems are shown together. Note that the 3D regions observed at different magnifications do not perfectly match owing to the difficulty in optical alignment; scale bars, 200 µm and 40 µm. (G) Three *z*-layers (difference, 20 µm) of the coronal plane of the local region of the choroid plexus. (H) Stereogram pair of isosurface representation of nuclei in a $(200\ \mu m)^3$ cubic volume.

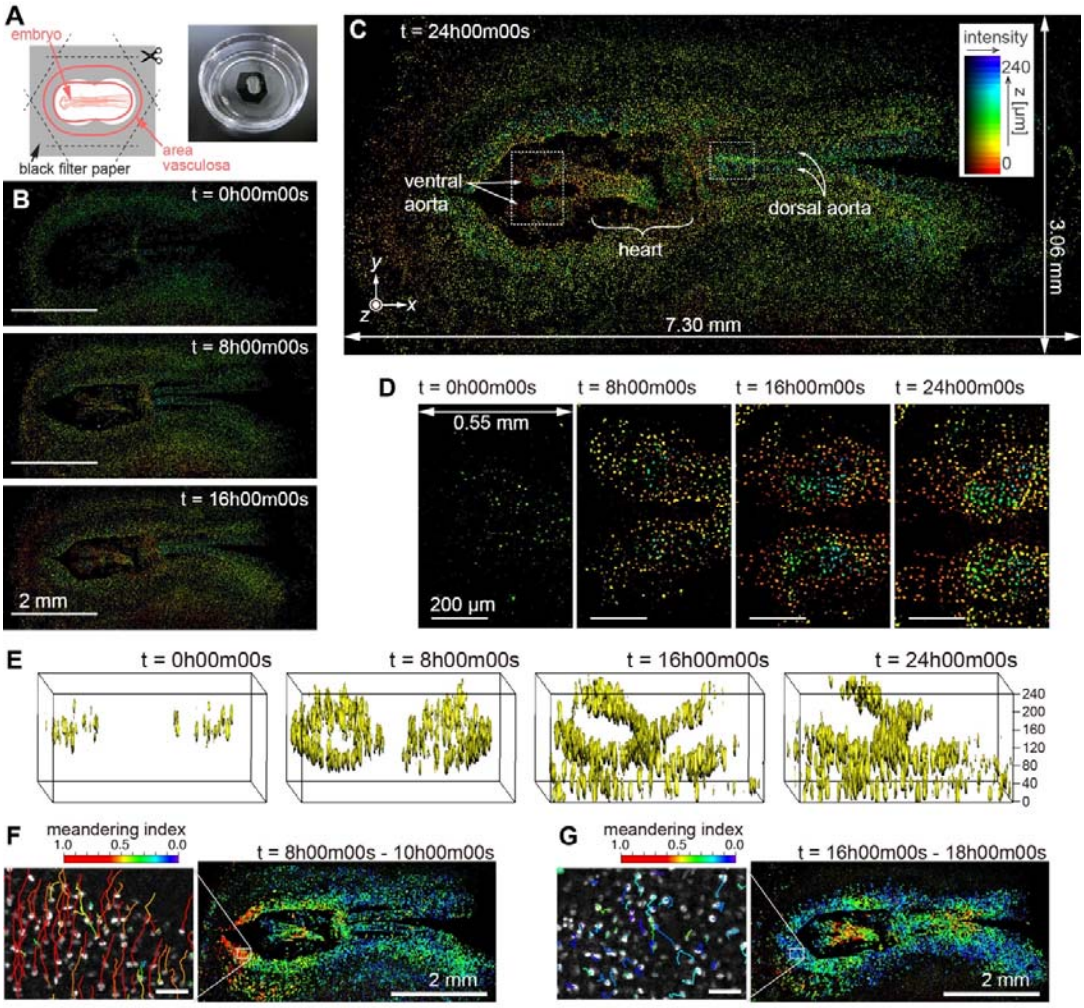

Fig. 5. Dynamics of vascular endothelial cells in quail embryo captured by time-lapse observation. (A) Schematic showing how the specimen is mounted (left) and a photograph of a specimen placed in a glass-bottom dish. (B) Representative images obtained at t = 0 h, 8 h, and 16 h; scale bars, 2 mm. (C) Enlarged view of the image corresponding at t = 24 h; the pseudo-colors represent the z-position of the cells and fluorescence intensity by their hue and brightness, respectively. (D) Magnified views of the anterior side of ventral aortae (left dashed square in (C)) at the four time-points with intervals of 8 h; scale bars, 200 μm. (E) Three-dimensional isosurface representation of the dorsal aorta region (right dashed square in (C)) viewed from the left side. (F),(G) Cell position trajectories and spatial mapping of features related to the cell dynamics in the two time-regions of (F) t = 8–10 h and (G) t = 16–18 h. Left panels show enlarged views in the white square regions (292 × 202 μm^2) indicated in the right panels. In both the panels, the rainbow-colored trajectories of the cell movement are overlaid on

the grayscale MIP images at the first frame in the time regions (F: t = 8 h, G: t = 16 h). The scale bars are 50 μm. The rainbow color table represents the meandering index of the cell movement in the two time-regions.